Accepted Manuscript

Electrical reduction of perovskite electrodes for accelerating exsolution of nanoparticles

Merika Chanthanumataporn, Jianing Hui, Xiangling Yue, Katsuyoshi Kakinuma, John T.S. Irvine, Katsunori Hanamura

PII: S0013-4686(19)30542-0

DOI: https://doi.org/10.1016/j.electacta.2019.03.126

Reference: EA 33842

To appear in: *Electrochimica Acta*

Received Date: 19 October 2018

Revised Date: 3 March 2019

Accepted Date: 18 March 2019

Please cite this article as: M. Chanthanumataporn, J. Hui, X. Yue, K. Kakinuma, J.T.S. Irvine, K. Hanamura, Electrical reduction of perovskite electrodes for accelerating exsolution of nanoparticles, *Electrochimica Acta* (2019), doi: https://doi.org/10.1016/j.electacta.2019.03.126.

Electrical Reduction of Perovskite Electrodes for Accelerating Exsolution of Nanoparticles

Merika Chanthanumataporn[a, *], Jianing Hui[b], Xiangling Yue[b], Katsuyoshi Kakinuma[c], John T.S. Irvine[b] and Katsunori Hanamura[a]

[a] *School of Engineering, Tokyo Institute of Technology, Ōokayama 2-12-1, Meguro-ku, Tokyo 152-8550, Japan.*

[b] *School of Chemistry, University of St Andrews, St Andrews, Fife, KY16 9ST Scotland, UK.*

[c] *Fuel Cell Nanomaterials Center, University of Yamanashi, Miyamae 6-43, Kofu, Yamanashi 400-0021, Japan.*

[*] Corresponding author. E-mail address: chanthanumataporn.m.aa@m.titech.ac.jp

Electrical Reduction of Perovskite Electrodes for Accelerating Exsolution of Nanoparticles

Growth of finely dispersed nanocatalysts by exsolution of metal nanoparticles from perovskite oxides under reducing conditions at elevated temperature is a promising approach of producing highly active catalytic materials. An alternative method of exsolution using an applied potential has been recently shown to potentially accelerate the exsolution process of nanoparticles that can be achieved in minutes rather than the hours required in chemical reduction. In the present study, we investigate exsolution of nanoparticles from perovskite oxides of $La_{0.43}Ca_{0.37}Ni_{0.06}Ti_{0.94}O_{3-\gamma}$ (LCTNi) and $La_{0.43}Ca_{0.37}Ni_{0.03}Fe_{0.03}Ti_{0.94}O_{3-\gamma}$ (LCTNi-Fe) under applied potentials in carbon dioxide atmosphere. The impedance spectra of single cells measured before and after electrochemical poling at varying voltages showed that the onset of exsolution process occurred at 2 V of potential reduction. An average particle size of the exsolved nanoparticles observed after testing using a scanning electron microscopy was about 30-100 nm. The cells with the reduced electrodes exhibited desirable electrochemical performances not only in pure carbon dioxide (current density of 0.37 A cm^{-2} for LCTNi and 0.48 A cm^{-2} for LCTNi-Fe at 1.5 V) but also in dry hydrogen (0.36 W cm^{-2} for LCTNi and 0.43 W cm^{-2} for LCTNi-Fe).

Keywords: Perovskite; Exsolution; Potential reduction; CO_2 electrolysis; Solid oxide cells

1. Introduction

Recently, exsolution of metal nanocatalysts from perovskite oxides at elevated temperature in reducing conditions has generated considerable research interest as a promising approach to produce perovskite materials with high catalytic properties [1–7]. In systems that demonstrate exsolution the desired catalyst, such as nickel, iron, cobalt, copper, palladium, rhodium, and platinum is substituted into the perovskite B-site in the typically oxidising conditions and subsequently released (exsolved) in the chosen reducing conditions, forming the metal nanoparticles at the perovskite oxide surface without the decomposition of the perovskite host [5]. In addition to their enhanced

catalytic activity, metal nanoparticles that are produced by exsolution have shown to be more resilient to agglomeration and coking compared to similar particles made by alternative methods due to their embedded structures within the perovskite substrates [4–6,8,9]. Applications where their enhanced catalytic properties were reported have been demonstrated in diverse areas of catalysis applications including solid oxide fuel cell (SOFC) and electrolysis cell (SOEC) electrodes [9–16].

An alternative method of exsolution using an applied potential under reducing SOEC cathode operating conditions has recently been reported in several studies [7,9,16]. A recent study by Myung *et al.* showed that nanoparticles could be produced through electrochemical poling at 2 V in minutes rather than the hours that are generally required in typical chemical reduction. This resulted in high performance electrodes that operated at 900 °C at 2 W/cm^2 in humidified H_2 and 2.75 A/cm^2 at 1.3 V in 50%H_2O/N_2 without degradation of the nanostructures and corresponding electrochemical activity after 150 hours of testing [16]. How performance of electrodes can be improved with the exsolution of nickel and iron nanoparticles during steam electrolysis was also demonstrated by Tsekouris *et al.* and Opitz *et al.* [7,9]. This electrochemical poling method is thus potentially useful for accelerating exsolution process of nanoparticles and enhancing the catalytic activity of solid oxide cell electrodes.

In this current study, we aim to investigate *in situ* preparation of perovskite electrodes with nanoparticle exsolution using an applied potential in an atmosphere of carbon dioxide. Particular emphasis will be placed on the impedance spectra of single cell measured before and after potential reducing (PR) at varying voltages in order to evaluate the appeal of the potential reduction for *in situ* producing high performance SOFC anodes and SOEC cathodes. The electrode compositions chosen for this study are $La_{0.43}Ca_{0.37}Ni_{0.06}Ti_{0.94}O_{3-\gamma}$ (LCTNi) and $La_{0.43}Ca_{0.37}Ni_{0.03}Fe_{0.03}Ti_{0.94}O_{3-\gamma}$ (LCTNi-Fe),

both of which have not been reported to produce nanoparticles under voltage in carbon dioxide atmosphere. The compositions will be reduced under varying potentials in pure carbon dioxide and evaluated their electrochemical performances as solid oxide fuel cell and electrolyser electrodes in dry hydrogen and carbon dioxide, respectively.

2. Experimental

2.1. Material synthesis and characterization

The perovskite $La_{0.43}Ca_{0.37}Ni_{0.06}Ti_{0.94}O_{3-\gamma}$ (LCTNi) and $La_{0.43}Ca_{0.37}Ni_{0.03}Fe_{0.03}Ti_{0.94}O_{3-\gamma}$ (LCTNi-Fe) powders were synthesized by a modified solid-state process [8,17]. High purity precursors including La_2O_3 (PI-KEM, 99.99%), TiO_2 (Sigma-Aldrich, anatase powder -325 mesh, ≥ 99% trace metals basis), $CaCO_3$ (Alfa-Aesar, 99.5% metal basis, 5 micro powder), $Ni(NO_3)_2{\cdot}6H_2O$ (ACROS Organics, 99%) and $Fe(NO_3)_3{\cdot}9H_2O$ (Sigma-Aldrich, ≥ 99.95% trace metals basis) were used as the raw materials in the appropriate stoichiometric ratios. The oxides and carbonate were dried at different temperatures (La_2O_3 at 850°C, TiO_2 and $CaCO_3$ at 350°C) for 2 h and weighed while warm. All the precursors, including nickel and iron nitrates, were quantitatively transferred to beakers and mixed with acetone and a small amount (~0.05 wt.%) of non-aqueous Hypermer KD-1 (polyester/polyamide copolymer) dispersant. The mixtures then undergo mixing using ultrasonic probe (Hielscher UP200S, operated at ~75% of maximum wave frequency an amplitude) in order to break down agglomerates. The correlated action of the dispersant and ultrasonic waves led to the formation of a fine, stable dispersion with better homogeneity compared to typical powder mixing in mortar and pestle used in solid state synthesis. The acetone is then evaporated under continuous stirring to ensure further homogenization. After the acetone was completely evaporated, the content of the beaker was quantitatively transferred into a crucible and then calcined at 1000 °C for 12

h in order to decompose the carbonates, remove adsorbed water and start the nucleation of the perovskite phase. After the calcination, the as-prepared powders were milled in acetone in a planetary ball mill at 200 rpm for 2 h. The corresponding powders were then pressed into pellets and sintered at 1400 ºC for 16 h to form the perovskite phase. Subsequently, the sintered pellets were ground thoroughly into powders to obtain LCTNi or LCTNi-Fe perovskite powders.

2.2. Cell fabrication

Button cell was fabricated by screen-printing electrode inks in an active area of 0.5 cm^2 on both sides of dense electrolyte support of 18 mm diameter. $Zr_{0.89}Sc_{0.1}Ce_{0.01}O_{2-\gamma}$ (ScSZ) electrolyte support (250 μm thickness after sintering) was fabricated by tape-casting and sintering at 1400 ºC. LCTNi and LCTNi-Fe inks were made by first dispersing the perovskite powders in acetone with 2 wt% Hypermer KD1 dispersant and ball-milling overnight (18-24 h). An organic vehicle (30 wt%), which consists of 5 wt% polyvinyl butyrate in terpineol, was then added into the slurry and the mixture was continuously stirred at room temperature overnight to completely evaporate acetone and yield the final inks. Through the same procedure, $(La_{0.8}Sr_{0.2})_{0.95}MnO_3$ (LSM)-ScSZ (50:50 wt%) ink was prepared. For the fuel electrode, the LCTNi or LCTNi-Fe ink was screen-printed first on one side of the dense ScSZ electrolyte and then fired at 1250 ºC, while for the air electrode, the LSM-ScSZ ink was screen-printed on the other side and followed by firing at 1100 ºC. The final thickness of both electrodes was about 13.5 μm after firing. Gold paste was applied in a radial pattern and contacted using gold wires for current collection and then fired at 750 ºC for 1 h to sinter it to the electrodes.

2.3. Electrochemical testing and characterization

The titanate electrode side, i.e. fuel electrode side, of solid oxide cell (SOC) was

mounted on alumina tube of testing jig and sealed with ceramic paste (Ceramabond 552, Aremco). The assembly was then placed in a vertical temperature-controlled furnace. An R-type thermocouple was placed close to the cell in order to monitor the cell operating temperature. The air electrode of the cell was always exposed to ambient air. After the system was heated up to the operating temperature at 900 ºC, 100% CO_2 at a constant flow rate of 50 mL/min was continuously introduced to the fuel electrode side for potential reduction (PR). For electrochemical evaluation, impedance and current-voltage (I-V) characteristics of the cell were measured and analyzed using a Solartron 1470B instrument. The potential reduction was performed by applying voltages range from 1.5 V to 2.2 V (in an order from low to high potential) under pure CO_2 atmosphere for 3, 10 and 20 minutes. Before and after each examined condition of the potential reduction, impedance data with AC voltage amplitude of 10 mV and frequency ranging from 10^5 Hz to 0.1 Hz were collected under open-circuit voltage (OCV) and as well as under condition of 1.35 V applied potential. Linear sweep voltammetry from 0 V to 2 V was then conducted to test the cell performance as CO_2 electrolyser. To evaluate the cell performance in fuel cell mode, the CO_2 was changed to dry 100% H_2. After stabilization in OCV condition, voltammetry was scanned from OCV to short circuit current at 0 V.

Following I–V and electrochemical impedance spectroscopy (EIS) measurements, the SOC was cooled to room temperature under dry 5% H_2/N_2 in order to maintain the titanate electrode in its reduced state, followed by destructive removal from the testing jig. SEM imaging was carried out using a Hitachi SU9000 scanning electron microscope (SEM). TEM sample preparation and analysis were carried out using a FB-2200 (Hitachi High technologies co., Japan) focused ion beam (FIB) and a HD-2700 (Hitachi High technologies co., Japan) scanning transmission electron

microscope (STEM) equipped an energy-dispersive X-ray spectroscopy (EDX, QUANTAX, Bruker, USA), respectively.

3. Results and discussion

3.1. Powder Characterization

Phase compositions of the prepared powders were identified using an X-ray diffractometer (PANalytical Empyrean) operated in reflection mode. Figure 1 shows XRD patterns of the as-prepared $La_{0.43}Ca_{0.37}Ni_{0.06}Ti_{0.94}O_{3-\gamma}$ (LCTNi) and $La_{0.43}Ca_{0.37}Ni_{0.03}Fe_{0.03}Ti_{0.94}O_{3-\gamma}$ (LCTNi-Fe) powders over a wide 2θ range. As shown in Fig. 1, the XRD patterns confirm both samples fit well to orthorhombic structure, without any secondary phase. A closer inspection of the reflections shows that the characteristic peak of LCTNi-Fe slightly shifts toward higher reflection angles compared to that of LCTNi. The peak shifting of LCTNi-Fe suggests that Ni^{2+} ion (ionic radius of 0.690 Å), was substituted by smaller Fe^{3+} ion (ionic radius of 0.645 Å) [9].

3.2. EIS Analysis

Exsolution of electrocatalytically active nanoparticles under voltage was investigated via EIS analysis at open circuit voltage (OCV) as well as 1.35 V applied potential in pure CO_2 atmosphere at 900 ºC. The impedance data obtained under OCV condition provides essential information of electrode material nature that is not governed by cell polarization under current flow, while the data at 1.35 V provides details under applied voltage condition, which is more similar to the practical operating conditions of SOCs. Figure 2(a) shows the open circuit EIS of the cell based on $La_{0.43}Ca_{0.37}Ni_{0.06}Ti_{0.94}O_{3-\gamma}$ (LCTNi) electrode measured before and after potential reduction (PR) at 1.5, 1.8, 2.0

and 2.2 V for 3 minutes. The impedance arc at high frequency and slightly depressed semi-circular arc at low frequency indicate two different electrode processes corresponding to the high- and low-frequency arcs exist. The equivalent circuit of ($LR_\Omega(R_1Q_1)(R_2Q_2)$) for the best fitting of all the impedance spectra have been achieved. R_Ω represents the ohmic resistance that is mainly contributed by the electrolyte resistance including the electrodes ohmic resistance, the contact resistance between the electrodes and electrolyte, and the leads resistance. The parallel circuit with resistance (R_1) and constant phase element (Q_1) that accounts for the depressed semi-circle at high frequency is associated with the charge-transfer process at the electrode/electrolyte interface. The low-frequency semi-circular arc (R_2Q_2) can be assigned to the gas adsorption and dissociation at the surface of the electrode [3,18,19]. The total polarization resistance of the single cell, R_p, can be expressed as the sum of R_1 and R_2. The inductance of the circuits, L, was added to consider the contribution of the high-frequency phase shift of the electrochemical equipment. The fitting results for the LCTNi electrode under OCV condition are listed in Table 1.

Table 1 EIS fitting values at OCV for LCTNi electrode before and after potential reduction (PR) at different voltages of 1.5, 1.8, 2.0 and 2.2 V for 3 minutes

	R_Ω (Ω cm^2)	R_1 (Ω cm^2)	R_2 (Ω cm^2)	R_p (Ω cm^2) [$R_p = R_1 + R_2$]
Before PR	1.40	8.741	126.02	134.76
1.5V PR	1.40	6.620	290.64	297.26
1.8V PR	1.24	2.874	324.36	327.24
2.0V PR	1.11	1.695	60.32	62.01
2.2V PR	1.08	1.287	25.76	27.05

As can be seen in Table 1, the ohmic resistance (R_Ω) of the cell measured at OCV decreases with the applied voltage of potential reduction from 1.40 Ω cm^2 before PR to 1.24, 1.11 and 1.08 Ω cm^2 after PR at 1.8, 2.0 and 2.2 V, respectively, indicating lower ohmic resistance of the electrode after the potential reduction. The polarization resistance (R_p) of the cell after potential reduction at 1.5 V and 1.8 V increases as the increment of the applied voltage, while after potential reduction at 2.0 V and 2.2 V R_p significantly decreases as the increment of the applied voltage. The significant increase or decrease in the total polarization resistance of the cell can be mainly contributed to the major change of the low-frequency impedance (R_2) as shown in Table 1, indicating the change of the electrochemical kinetics of the electrode associated to the activation of chemical processes at the electrode surface. The remarkable reduction of the cell polarization resistance after potential reduction at 2.0 V clearly reflects onset of significant exsolution, whereas increase of R_p after PR at 1.5 V (or 1.8 V) shows process becomes more difficult as current increases, which indicates starvation of active sites due to increased current.

The major increase of low-frequency impedance, which resulted in the increases of R_p after potential reduction at 1.5 V and 1.8 V, indicates a significant resistance to CO_2 conversion (eqn (1)) at the surface of the electrode. The electrochemical dissociation of CO_2 to CO occurring at the electrode surface is expressed by using the Kröger–Vink notation for defects [20], which the conversion reaction of CO_2 is accompanied by the formation of oxygen ions and the simultaneous consumption of oxygen vacancies:

$$CO_2 + V_O^{\cdot\cdot} + 2e^- = CO + O_O^{\times} \quad (1)$$

The fact that the low-frequency impedance of the electrode increases significantly after

potential reduction at 1.5 V and 1.8 V suggests that the surface reaction of CO_2 adsorption and/or reduction is difficult to occur after being reduced at this voltage range due to the starvation of active sites, such as vacant sites for oxide ion migration, and sites available for the adsorption of reactant CO_2 molecules. From the results, it is likely that significant resistance or enhancement of the CO_2 conversion depending on applied voltage of the reduction is associated with change of the concentration of oxygen vacancies in the electrode upon reduction [9,21]. At the sufficient applied potential the electrochemical kinetics become facile, which the entire LCTNi grain is reduced to a limit in number of introduced oxygen vacancies, resulting in exsolution of electrocatalytically active nanoparticles [9]. The presence of metal nanocatalysts and higher oxygen vacancy concentrations in the lattice yield increased oxide ion mobility and availability of adsorption sites, accounting for the remarkable reduction of the polarization resistance after potential reduction at 2.0 V.

Table 2 EIS fitting values at 1.35 V for LCTNi electrode before and after potential reduction for 3 minutes at different voltages of 1.5, 1.8, 2.0 and 2.2 V; and for different annealing time of 3, 10 and 20 minutes at 2.0 V

	R_Ω (Ω cm^2)	R_1 (Ω cm^2)	R_2 (Ω cm^2)	R_p (Ω cm^2) [$R_p = R_1 + R_2$]
Before PR	0.494	0.243	5.474	5.717
1.5V PR_3min	0.491	0.246	5.177	5.423
1.8V PR_3min	0.438	0.232	3.501	3.733
2.0V PR_3min	0.392	0.160	1.082	1.241
2.0V PR_10min	0.386	0.140	0.844	0.984
2.0V PR_20min	0.381	0.131	0.770	0.900
2.2V PR_3min	0.381	0.121	0.687	0.808

The impedance data of the cell with the LCTNi electrode measured under an applied voltage of 1.35 V before and after PR for 3 minutes at 1.5, 1.8, 2.0 and 2.2 V; and for 3, 10 and 20 minutes at 2.0 V are shown in Fig. 2(b). The fitted impedance values examined at 1.35 V are summarized in Table 2. Comparing both ohmic and polarization resistances in Table 1 and Table 2, the impedances at 1.35 V, R_p in particular, are significantly lower than those measured at OCV due to the increased voltage condition. As can be seen in Fig. 2(b), the ohmic and polarization resistances of the cell measured at 1.35 V after potential reduction decrease as the increment of the applied voltage as well as the PR duration. From the Table 2, small decreases in polarization resistances after potential reduction at 1.5 and 1.8 V were observed (5% and 35%, respectively). However, after potential reduction at 2.0 V, the R_p remarkably decreases (78%) and then reduces more 35% after PR at 2.2 V for 3 minutes. The significant decrease of R_p after PR at 2.0 V measured at 1.35 V further confirms the onset of exsolution process at 2 V of potential reduction, whereas the effect of resistant layer, which resulted in the increased R_2 observed under OCV, was mediated by the increased oxygen vacancy concentration under applied potential condition in mixed conducting materials [22]. As shown in Fig. 2b, the ohmic resistances after PR at 2.0 V for 3 min (0.392 Ω cm^2), 10 min (0.386 Ω cm^2) and 20 min (0.381 Ω cm^2) are close to each other, while the polarization resistance noticeably decreases as the duration of potential reduction increases. From the plot, it appears that the R_p of the cell after PR for 10min (0.984 Ω cm^2) and 20 min (0.900 Ω cm^2) are slightly different, whereas longer applied voltage of PR from 3 min to 10 min shows an obvious decrease in the cell polarization resistance (1.241 and 0.984 Ω cm^2, respectively).

Ni-Fe bimetallic nanoparticles that has been previously demonstrated to produce by exsolution in a reducing condition are of interest due to their better resistance to

carbon deposition compared to Ni monometallic nanoparticles [3]. In comparison with LCTNi, $La_{0.43}Ca_{0.37}Ni_{0.03}Fe_{0.03}Ti_{0.94}O_{3-\gamma}$ (LCTNi-Fe) was also investigated to produce alloy nanoparticles under voltage. Figure 3 shows the EIS comparison of the cells with the LCTNi and LCTNi-Fe electrodes measured in dry CO_2 atmosphere at 900 ºC under OCV (Fig. 3(a)) and 1.35 V (Fig. 3(b)) conditions. From the plots, similar impedance behaviours after potential reduction for the LCTNi and LCTNi-Fe electrodes were observed in all cases. Figure 3(a) shows the open circuit EIS of the LCTNi-Fe and LCTNi before and after PR at 2.0 and 2.2 V for 3. The EIS fitting results for the LCTNi-Fe at OCV are also given in Table 3. As listed in Table 3, the cell ohmic resistance at OCV for the LCTNi-Fe does not change after potential reduction at 2.0 V, while after potential reduction at 2.2 V R_Ω decreases 10%. The polarization resistance at OCV for the LCTNi-Fe changes with the applied voltage of potential reduction, remarkably decreasing by five times before (287.5 Ω cm^2) and after PR at 2.0 V (58.42 Ω cm^2) and reaching the minimum value after PR at 2.2 V (41.11 Ω cm^2). From Fig. 3(a), it appears that, not only for LCTNi but also for LCTNi-Fe, 2 V of potential reduction is the onset for significant exsolution under voltage corresponding to the considerable decrease in R_p at 2 V.

Table 3 EIS fitting values at OCV for LCTNi-Fe electrode before and after potential reduction (PR) at 2.0 and 2.2 V for 3 minutes

	R_Ω (Ω cm^2)	R_1 (Ω cm^2)	R_2 (Ω cm^2)	R_p (Ω cm^2) [$R_p = R_1 + R_2$]
Before PR	1.53	5.866	281.64	287.50
2.0V PR	1.53	1.918	56.50	58.42
2.2V PR	1.37	0.835	40.28	41.11

Comparing R_Ω and R_p values measured at OCV for the same conditions in Table 1 (LCTNi) and Table 3 (LCTNi-Fe), the ohmic resistance for the LCTNi-Fe is always higher than R_Ω for the LCTNi (9% before PR, 38% after PR at 2.0 V and 27% after PR at 2.2 V). The polarization resistance for the LCTNi-Fe is two times higher than that for the LCTNi before PR, whereas R_p for the LCTNi-Fe is 6% lower and 1.5 times higher than R_p for the LCTNi after the cells were applied with voltage at 2.0 and 2.2 V, respectively. Figure 3(b) shows the impedance spectroscopy of the LCTNi-Fe and LCTNi electrodes measured at 1.35 V in pure CO_2 at 900ºC after potential reduction at 2.0 V for 3 and 20 minutes; and at 2.2 V for 3 minutes. From Table 4, which the fitted impedance results for LCTNi-Fe electrode at 1.35 V are given, R_Ω for the LCTNi-Fe barely changes with the applied voltage of potential reduction, while R_p decreases with the applied voltage as well as the PR duration, which shows the same tendency of impedance behaviours observed in LCTNi. Comparing R_Ω and R_p values at 1.35 V after potential reduction in Table 2 (LCTNi) and Table 4 (LCTNi-Fe), the ohmic resistance for the LCTNi-Fe is slightly lower ($\leq$ 4%) compared to that for the LCTNi, whereas the polarization resistance for the LCTNi-Fe is significantly lower than that for the LCTNi in the same condition.

Table 4 EIS fitting values at 1.35 V for LCTNi-Fe electrode after potential reduction at 2.0 V for 3 and 20 minutes; and at 2.2 V for 3 minutes

	R_Ω (Ω cm^2)	R_1 (Ω cm^2)	R_2 (Ω cm^2)	R_p (Ω cm^2) [$R_p = R_1 + R_2$]
2.0V PR_3min	0.376	0.117	0.761	0.878
2.0V PR_20min	0.370	0.095	0.631	0.726
2.2V PR_3min	0.372	0.090	0.582	0.672

3.3. Nanoparticle characterization

Figure 4 shows SEM images of fresh LCTNi electrode before potential reduction (Fig. 4(a)), and the reduced LCTNi (Fig. 4(b)) and LCTNi-Fe (Fig. 4(c)) electrodes after electrochemical performance testing at 900 ºC. As can be seen in Fig. 4(a), the surface of perovskite was shown to consist of steps and ledges corresponding to low index crystallographic planes. This terraced morphology is common to see in A-site deficient titanate perovskites [5]. From the images, it is evident that the unreduced LCTNi clearly shows no evidence of any nanoparticles on the surface (Fig. 4(a)), whereas after potential reduction nanoparticles with diameter of ~30-100 nm were readily apparent on the LCTNi (Fig. 4(b)) and LCTNi-Fe (Fig. 4(c)) surfaces.

Figure 5(a) and (b) shows STEM images of the exsolved nanoparticles on the surfaces of the reduced LCTNi and LCTNi-Fe (Fig. 5(a) and (b), respectively), which the particles are apparently to be embedded within the perovskite substrates. The observed particles and substrates in Fig. 5 were covered with an outer shell of an oxide layer, which is an artifact that formed after the electrodes were exposed to air for a long time. A composition analysis of the surface nanoparticles was further performed using the TEM-EDS and the results were shown in Fig. 5(c) and (d) for the reduced LCTNi and LCTNi-Fe, respectively. Strong peaks of Ni signal obtained from the particle exsolved from the LCTNi substrate (Fig. 5(c)) confirm the exsolution of Ni nanoparticles, while the relatively strong peaks of Ni and Fe obtained from particle on the reduced LCTNi-Fe surface (Fig. 5(d)) indicate the presence of Ni-Fe alloy. From Fig. 5(c) and (d), it can be seen that an artifact of gold were also observed from the spectra of the surface particles, which in this study gold was applied as an inert current collector.

3.4. Single cell performance

The electrochemical performance of a single cell with the LCTNi or LCTNi-Fe electrode was evaluated at 900 ºC after the EIS analysis was performed. Figure 6 shows the typical current-voltage plots of a single cell consisting of $(La_{0.8}Sr_{0.2})_{0.95}MnO_3$-$Zr_{0.89}Sc_{0.1}Ce_{0.01}O_{2-\gamma}$ (LSM-ScSZ) air-electrode, ScSZ electrolyte and the LCTNi or LCTNi-Fe fuel-electrode operating at 900 ºC in 100% CO_2 for electrolysis mode (Fig. 6(a)) and in dry H_2 for fuel-cell mode (Fig. 6(b)). Negative and positive currents indicate the reduction of carbon dioxide and the oxidation of hydrogen, respectively. In Fig. 6(a), the OCV values of the cells with the LCTNi and LCTNi-Fe electrodes are 0.12 V and 0.21 V, respectively. The I-V curve enters into the ohmic regime (indicated by the fitted straight line) with a slope change at approximately 1.2 V for the LCTNi and 1.1 V for the LCTNi-Fe. The slopes of the I-V curves in the ohmic regime that reflect the internal resistances of the cells with the LCTNi and LCTNi-Fe electrodes are 0.84 Ω cm^2 and 0.81 Ω cm^2, respectively. At 1.5 V the (absolute) current density of the cells with the LCTNi and LCTNi-Fe electrodes are 0.37 and 0.48 A cm^{-2}, respectively. The higher current efficiency of the cell with the LCTNi-Fe is consistent with the impedance results obtained at 1.35 V in which the LCTNi-Fe has the lower polarization resistance compared to that of the cell with the LCTNi. The current densities of the single cells measured under direct CO_2 electrolysis condition in this study (0.37 A cm^{-2} for LCTNi and 0.48 A cm^{-2} for LCTNi-Fe at 1.5 V, 900 ºC) are comparable to those recently reported perovskite titanate electrodes with nickel nanoparticles that were produced by exsolution in a reducing hydrogen atmosphere [1,2]. Li *et al.* demonstrated the current density at 1.5 V of the electrolyser based on the $(La_{0.2}Sr_{0.8})_{0.9}(Ti_{0.9}Mn_{0.1})_{0.9}Ni_{0.1}O_{3-\delta}$/YSZ cathode with exsolved Ni nanoparticles was 0.07 A cm^{-2} in 100% CO_2 at 800 ºC [1]. Gan *et al.* achieved a better performance with

the current density at 1.5 V in 100% CO_2 reached 0.165 A cm^{-2} at 800 ºC with $(La_{0.3}Sr_{0.7})Ti_{0.95}Ni_{0.05}O_{3-\delta}/Ce_{0.8}Sm_{0.2}O_{2-\delta}$ as cathode [2].

Figure 6(b) shows the I-V and powder density curves of the single cell with the LCTNi or LCTNi-Fe electrode measured at 900 ºC in dry H_2. The OCV values of 1.12 V for the LCTNi and 1.15 V for the LCTNi-Fe were observed indicating satisfying separation between the anodic and cathodic chambers. The maximum power density of the cell with the LCTNi electrode operating in dry H_2 was 0.36 W cm^{-2}, whereas the cell with the LCTNi-Fe electrode achieved the higher maximum power density of 0.43 W cm^{-2}. These values are comparable to those reported at lower temperature for the cells with $Ce_{0.7}Sr_{0.1}Ni_{0.2}VO_3$-YSZ (0.31 W cm^{-2} at 700 ºC) [15], $La_{0.8}Sr_{0.2}Cr_{0.82}Ru_{0.18}O_{3-\delta}$-GDC (0.39 W cm^{-2} at 800 ºC) [10] and $La_{0.8}Sr_{0.2}Cr_{0.69}Ni_{0.18}O_{3-\delta}$-GDC (0.364 W cm^{-2} at 800 ºC) [23] anodes testing in humidified H_2. From Figure 6, it appears that the LCTNi-Fe demonstrates the better electrochemical performances and catalytic activities for not only the reduction of carbon dioxide but also the oxidation of hydrogen compared to the LCTNi.

The enhancement of catalytic performance of material due to the improvement of electrical conductivity following the promotion of the material reducibility by adding Fe has previously been reported by Sun *et al.* [3]. In that study, the Ni- and Fe co-doped $LaSrCrO_3$ (LSC) bimetallic perovskite anode with the exsolved Ni-Fe alloy nanoparticles that were produced in a reducing atmosphere showed better electrochemical performances in both 5000 ppm H_2S-H_2 and syngas compared to a Ni monometallic anode. This results of the better catalytic property of the electrode material with the exsolved Ni-Fe alloy is consistent with our experimental results in which the LCTNi-Fe demonstrates the better electrochemical performances compared to the LCTNi.

4. Conclusions

The perovskite electrodes of $La_{0.43}Ca_{0.37}Ni_{0.06}Ti_{0.94}O_{3-\gamma}$ (LCTNi) and $La_{0.43}Ca_{0.37}Ni_{0.03}Fe_{0.03}Ti_{0.94}O_{3-\gamma}$ (LCTNi-Fe) were investigated to produce nanoparticles by exsolution under voltage in carbon dioxide atmosphere. The impedance spectra of single cells measured before and after electrical reducing showed that 2 V of potential reduction was the onset for significant exsolution under voltage. The exsolution of nanoparticles with an average particle size of ~30-100 nm was observed on the reduced perovskite surfaces using SEM. The cells with the reduced LCTNi and LCTNi-Fe electrodes exhibited the current density at 1.5 V in 100% CO_2 of 0.37 and 0.48 A cm^{-2}, respectively. The maximum power density of the cell operating in dry H_2 was 0.36 W cm^{-2} for LCTNi and 0.43 W cm^{-2} for LCTNi-Fe. The desirable electrochemical performance results in both electrolysis and fuel cells suggested that the electrical reduction could be potentially useful for accelerating exsolution of active nanoparticles and instantly producing high performance SOFC anodes and SOEC cathodes.

Acknowledgements

This work was supported through the Leading Graduate School Program: Academy for Co-creative Education of Environment and Energy Science (ACEEES) funded by the Ministry of Education, Culture, Sports, Science and Technology (MEXT, Japan).

References

[1] Y. Li, K. Xie, S. Chen, H. Li, Y. Zhang, Y. Wu, Efficient Carbon Dioxide Electrolysis Based on Perovskite Cathode Enhanced with Nickel Nanocatalyst, Electrochimica Acta. 153 (2015) 325–333. doi:10.1016/j.electacta.2014.11.151.

[2] L. Gan, L. Ye, S. Tao, K. Xie, Titanate cathodes with enhanced electrical properties achieved via growing surface Ni particles toward efficient carbon dioxide electrolysis, Phys. Chem. Chem. Phys. 18 (2016) 3137–3143. doi:10.1039/C5CP06742A.

[3] Y.-F. Sun, J.-H. Li, L. Cui, B. Hua, S.-H. Cui, J. Li, J.-L. Luo, A-site-deficiency facilitated in situ growth of bimetallic Ni–Fe nano-alloys: a novel coking-tolerant

fuel cell anode catalyst, Nanoscale. 7 (2015) 11173–11181. doi:10.1039/C5NR02518D.

[4] Y. Nishihata, J. Mizuki, T. Akao, H. Tanaka, M. Uenishi, M. Kimura, T. Okamoto, N. Hamada, Self-regeneration of a Pd-perovskite catalyst for automotive emissions control, Nature. 418 (2002) 164–167. doi:10.1038/nature00893.

[5] D. Neagu, G. Tsekouras, D.N. Miller, H. Ménard, J.T.S. Irvine, In situ growth of nanoparticles through control of non-stoichiometry, Nat. Chem. 5 (2013) 916–923. doi:10.1038/nchem.1773.

[6] H. Tanaka, M. Uenishi, M. Taniguchi, I. Tan, K. Narita, M. Kimura, K. Kaneko, Y. Nishihata, J. Mizuki, The intelligent catalyst having the self-regenerative function of Pd, Rh and Pt for automotive emissions control, Catal. Today. 117 (2006) 321–328. doi:10.1016/j.cattod.2006.05.029.

[7] A.K. Opitz, A. Nenning, C. Rameshan, R. Rameshan, R. Blume, M. Hävecker, A. Knop□Gericke, G. Rupprechter, J. Fleig, B. Klötzer, Enhancing Electrochemical Water-Splitting Kinetics by Polarization-Driven Formation of Near-Surface Iron(0): An In Situ XPS Study on Perovskite-Type Electrodes, Angew. Chem. Int. Ed. 54 (n.d.) 2628–2632. doi:10.1002/anie.201409527.

[8] D. Neagu, T.-S. Oh, D.N. Miller, H. Ménard, S.M. Bukhari, S.R. Gamble, R.J. Gorte, J.M. Vohs, J.T.S. Irvine, Nano-socketed nickel particles with enhanced coking resistance grown in situ by redox exsolution, Nat. Commun. 6 (2015) 8120. doi:10.1038/ncomms9120.

[9] G. Tsekouras, D. Neagu, J.T.S. Irvine, Step-change in high temperature steam electrolysis performance of perovskite oxide cathodes with exsolution of B-site dopants, Energy Environ. Sci. 6 (2013) 256–266. doi:10.1039/C2EE22547F.

[10] B.D. Madsen, W. Kobsiriphat, Y. Wang, L.D. Marks, S.A. Barnett, Nucleation of nanometer-scale electrocatalyst particles in solid oxide fuel cell anodes, J. Power Sources. 166 (2007) 64–67. doi:10.1016/j.jpowsour.2006.12.080.

[11] W. Kobsiriphat, B.D. Madsen, Y. Wang, L.D. Marks, S.A. Barnett, La0.8Sr0.2Cr1−xRuxO3−δ–Gd0.1Ce0.9O1.95 solid oxide fuel cell anodes: Ru precipitation and electrochemical performance, Solid State Ion. 180 (2009) 257–264. doi:10.1016/j.ssi.2008.12.022.

[12] T. Jardiel, M.T. Caldes, F. Moser, J. Hamon, G. Gauthier, O. Joubert, New SOFC electrode materials: The Ni-substituted LSCM-based compounds (La0.75Sr0.25)(Cr0.5Mn0.5−xNix)O3−δ and (La0.75Sr0.25)(Cr0.5−xNixMn0.5)O3−δ, Solid State Ion. 181 (2010) 894–901. doi:10.1016/j.ssi.2010.05.012.

[13] D.M. Bierschenk, E. Potter-Nelson, C. Hoel, Y. Liao, L. Marks, K.R. Poeppelmeier, S.A. Barnett, Pd-substituted (La,Sr)CrO3−δ–Ce0.9Gd0.1O2−δ solid oxide fuel cell anodes exhibiting regenerative behavior, J. Power Sources. 196 (2011) 3089–3094. doi:10.1016/j.jpowsour.2010.12.050.

[14] B.D. Madsen, W. Kobsiriphat, Y. Wang, L.D. Marks, S. Barnett, SOFC Anode Performance Enhancement through Precipitation of Nanoscale Catalysts, ECS Trans. 7 (2007) 1339–1348. doi:10.1149/1.2729237.

[15] L. Adijanto, V.B. Padmanabhan, R. Küngas, R. J. Gorte, J. M. Vohs, Transition metal-doped rare earth vanadates: a regenerable catalytic material for SOFC anodes, J. Mater. Chem. 22 (2012) 11396–11402. doi:10.1039/C2JM31774E.

[16] J. Myung, D. Neagu, D.N. Miller, J.T.S. Irvine, Switching on electrocatalytic activity in solid oxide cells, Nature. 537 (2016) 528–531. doi:10.1038/nature19090.

[17] D. Neagu, J.T.S. Irvine, Enhancing Electronic Conductivity in Strontium Titanates through Correlated A and B-Site Doping, Chem. Mater. 23 (2011) 1607–1617. doi:10.1021/cm103489r.
[18] C.J. Fu, S.H. Chan, X.M. Ge, Q.L. Liu, G. Pasciak, A promising Ni–Fe bimetallic anode for intermediate-temperature SOFC based on Gd-doped ceria electrolyte, Int. J. Hydrog. Energy. 36 (2011) 13727–13734. doi:10.1016/j.ijhydene.2011.07.119.
[19] S.D. Ebbesen, M. Mogensen, Electrolysis of carbon dioxide in Solid Oxide Electrolysis Cells, J. Power Sources. 193 (2009) 349–358. doi:10.1016/j.jpowsour.2009.02.093.
[20] F.A. Kroger, H.J. Vink, Solid state physics, Seitz F Turnbull Ed. 3 (1956).
[21] Y.L. Yang, A.J. Jacobson, C.L. Chen, G.P. Luo, K.D. Ross, C.W. Chu, Oxygen exchange kinetics on a highly oriented La0.5Sr0.5CoO3−δ thin film prepared by pulsed-laser deposition, Appl. Phys. Lett. 79 (2001) 776–778. doi:10.1063/1.1390316.
[22] S.B. Adler, J.A. Lane, B.C.H. Steele, Electrode Kinetics of Porous Mixed□ Conducting Oxygen Electrodes, J. Electrochem. Soc. 143 (1996) 3554–3564. doi:10.1149/1.1837252.
[23] W. Kobsiriphat, B.D. Madsen, Y. Wang, M. Shah, L.D. Marks, S.A. Barnett, Nickel- and Ruthenium-Doped Lanthanum Chromite Anodes: Effects of Nanoscale Metal Precipitation on Solid Oxide Fuel Cell Performance, J. Electrochem. Soc. 157 (2010) B279–B284. doi:10.1149/1.3269993.
[24] Z. Zhang, G.R. Lumpkin, C.J. Howard, K.S. Knight, K.R. Whittle, K. Osaka, Structures and phase diagram for the system CaTiO3–La2/3TiO3, J. Solid State Chem. 180 (2007) 1083–1092. doi:10.1016/j.jssc.2007.01.005.

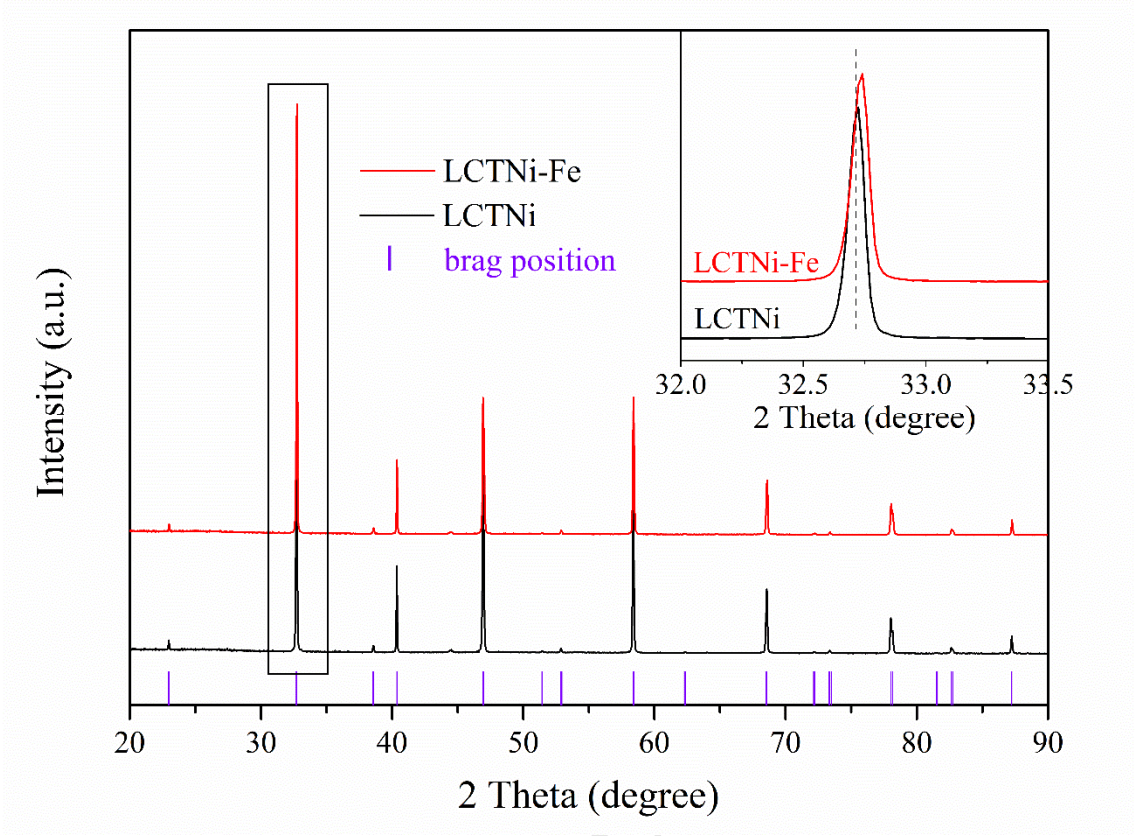

Figure 1. XRD patterns of the as-prepared $La_{0.43}Ca_{0.37}Ni_{0.06}Ti_{0.94}O_{3-\gamma}$ (LCTNi) and $La_{0.43}Ca_{0.37}Ni_{0.03}Fe_{0.03}Ti_{0.94}O_{3-\gamma}$ (LCTNi-Fe) powders over a wide 2θ range [24]

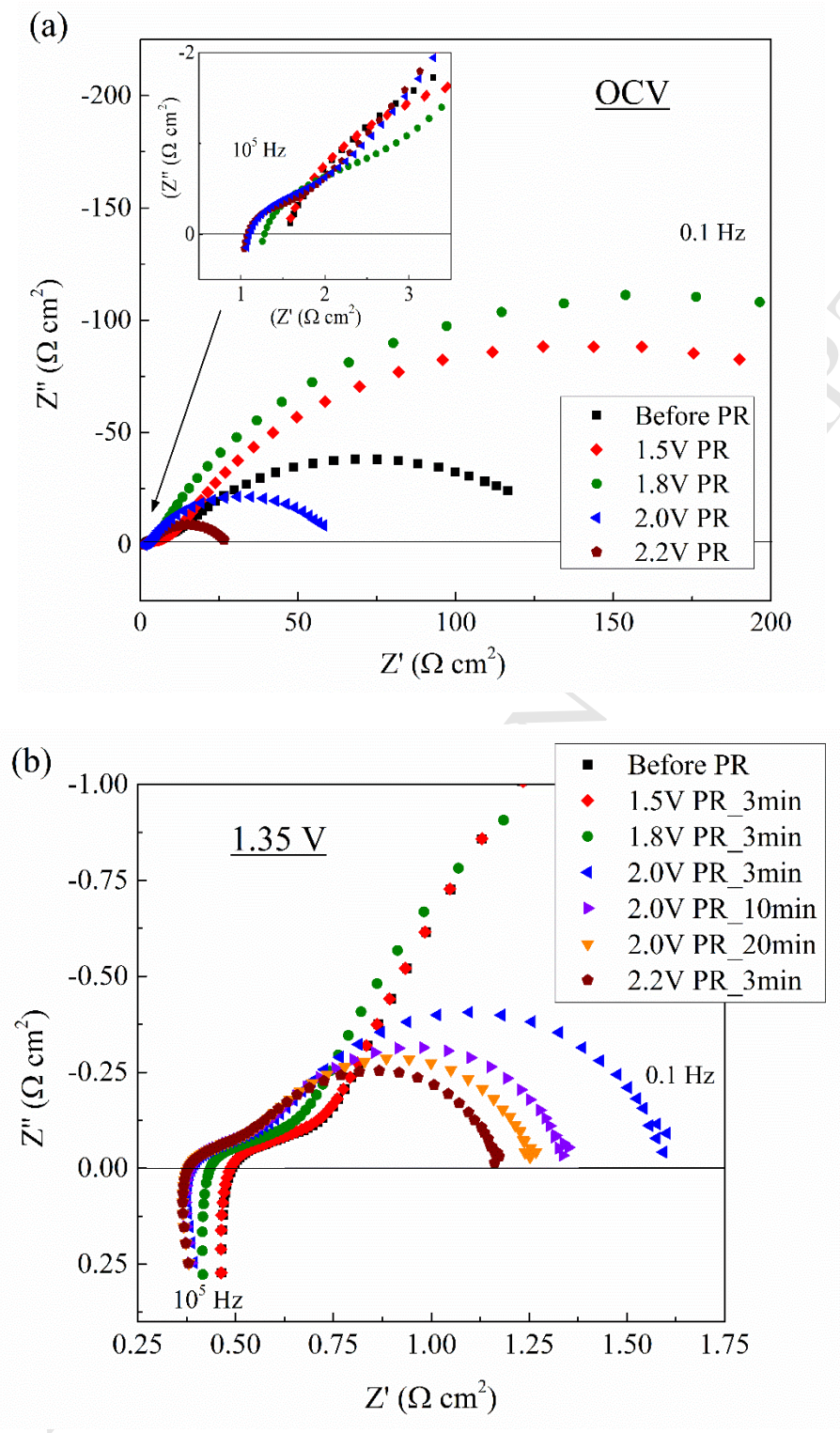

Figure 2. Impedance spectra of a single cell with LCTNi electrode working in pure CO2 atmosphere at 900ºC (a) Open circuit EIS before and after potential reduction (PR) at 1.5, 1.8, 2.0 and 2.2 V for 3 minutes and (b) EIS at 1.35 V before and after potential reduction for 3 minutes at different voltages of 1.5, 1.8, 2.0 and 2.2 V; and for different duration of 3, 10 and 20 minutes at 2.0 V

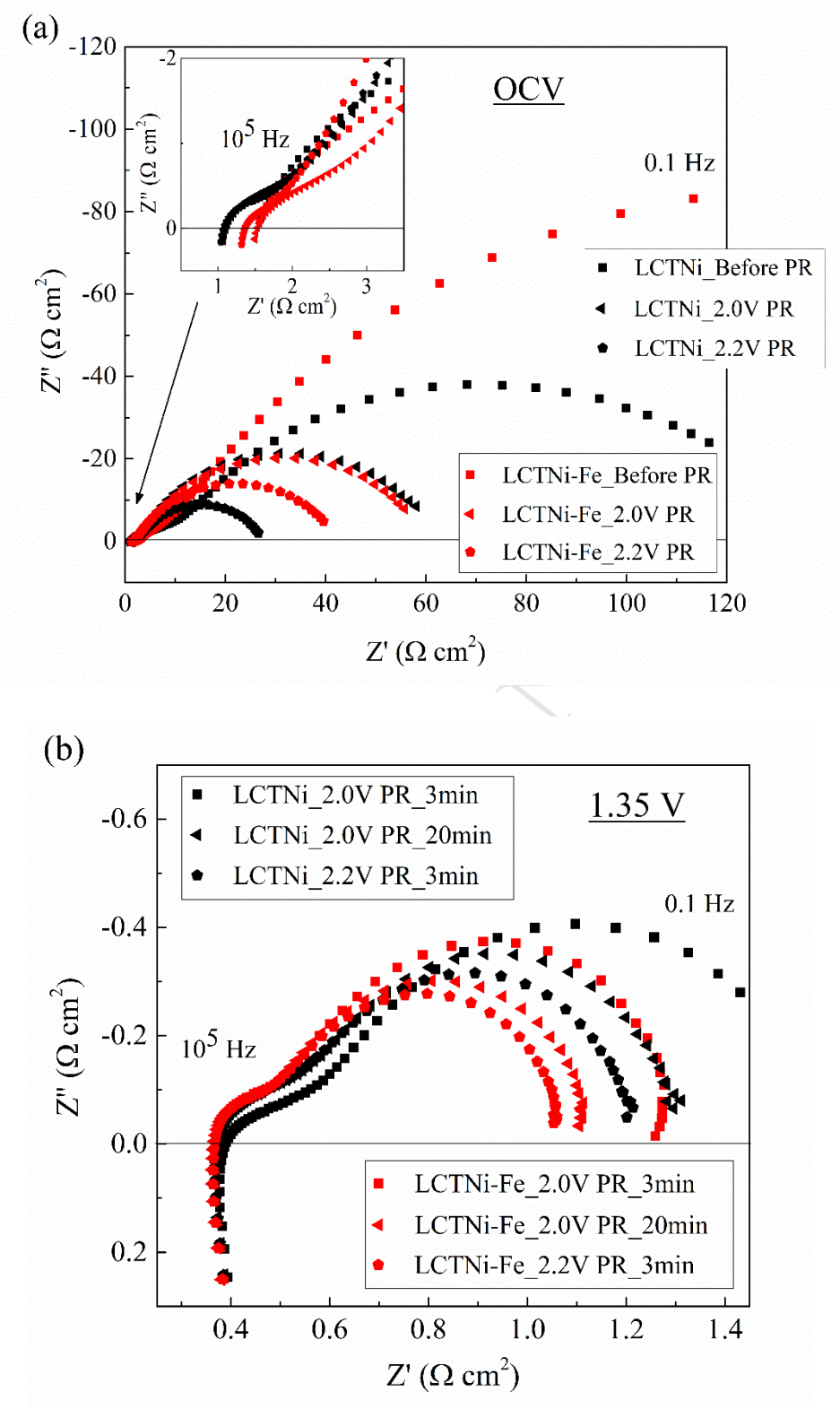

Figure 3. Impedance spectra of SOCs based on LCTNi and LCTNi-Fe electrodes working in pure CO_2 atmosphere at 900 ºC (a) Open circuit EIS before and after potential reduction (PR) at 2.0 and 2.2 V for 3 minutes (b) EIS at 1.35 V after potential reduction at 2.0 V for 3 and 20 minutes; and at 2.2 V for 3 minutes

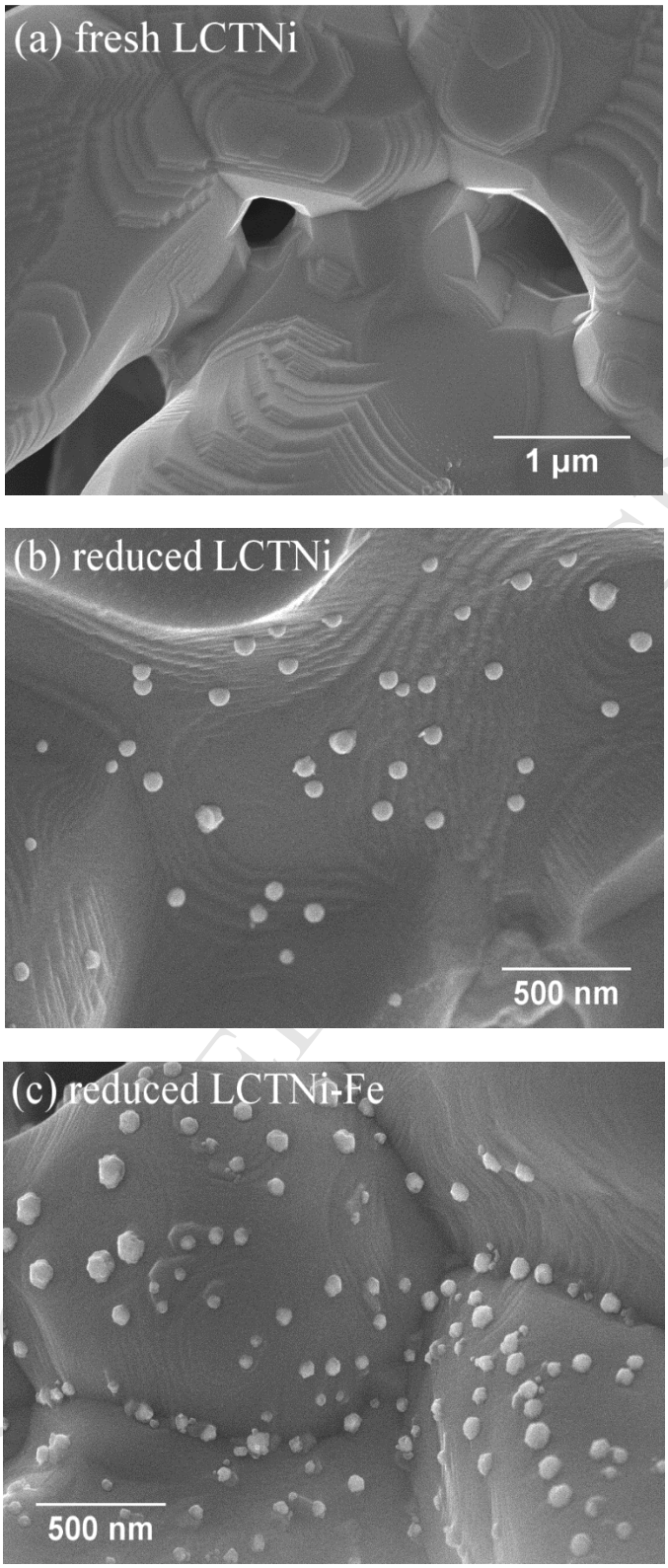

Figure 4. Scanning electron images of (a) fresh LCTNi before potential reduction. (b) reduced LCTNi and (c) reduced LCTNi-Fe after potential reduction showing the resultant nanoparticles grown on the surfaces.

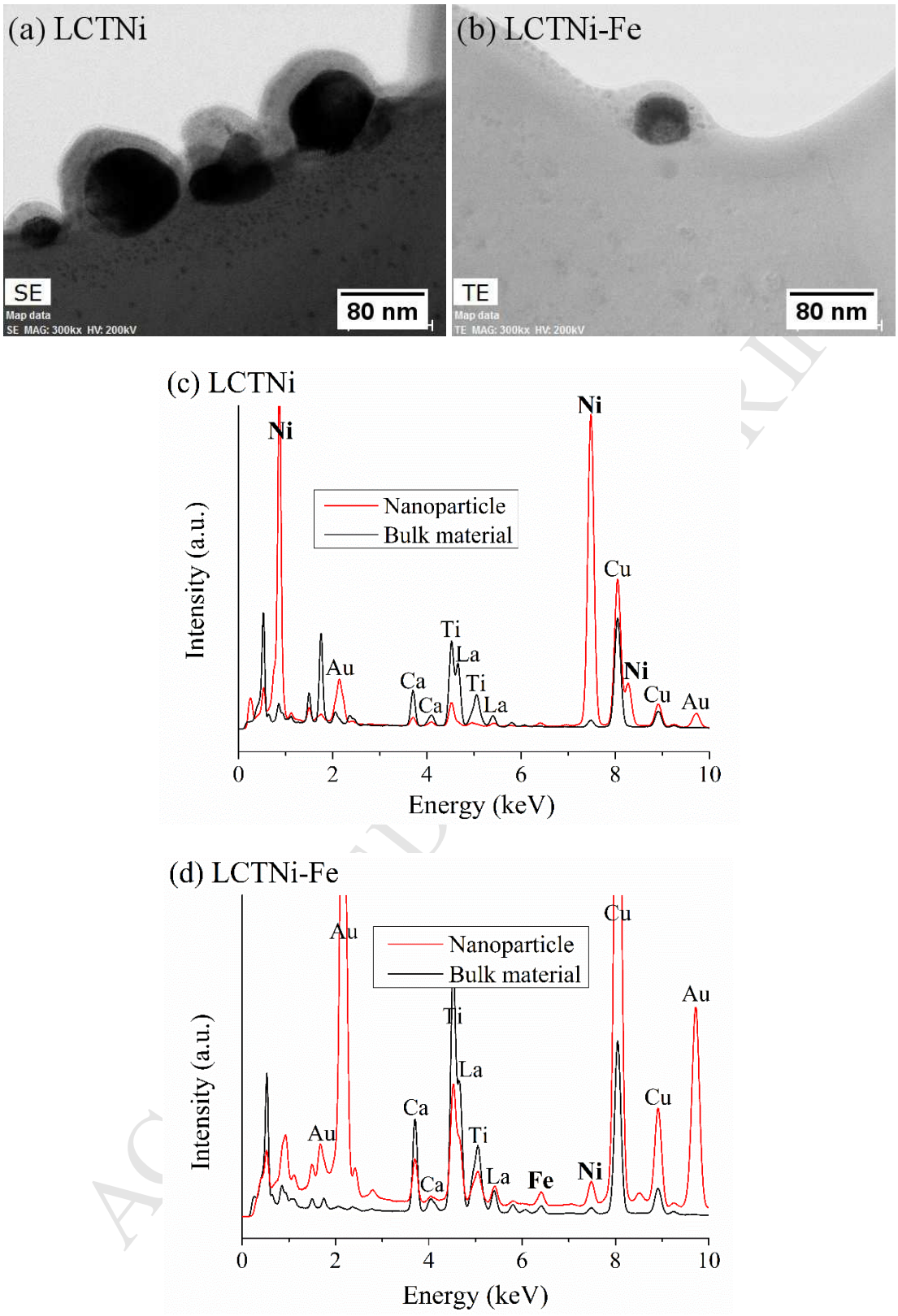

Figure 5. (a), (b) Scanning transmission electron images of exsolved nanoparticles on surfaces of (a) reduced LCTNi and (b) reduced LCTNi-Fe. (c), (d) TEM-EDS analysis of surface nanoparticles for (c) reduced LCTNi and (d) reduced LCTNi-Fe. (Supplementary Fig. S2)

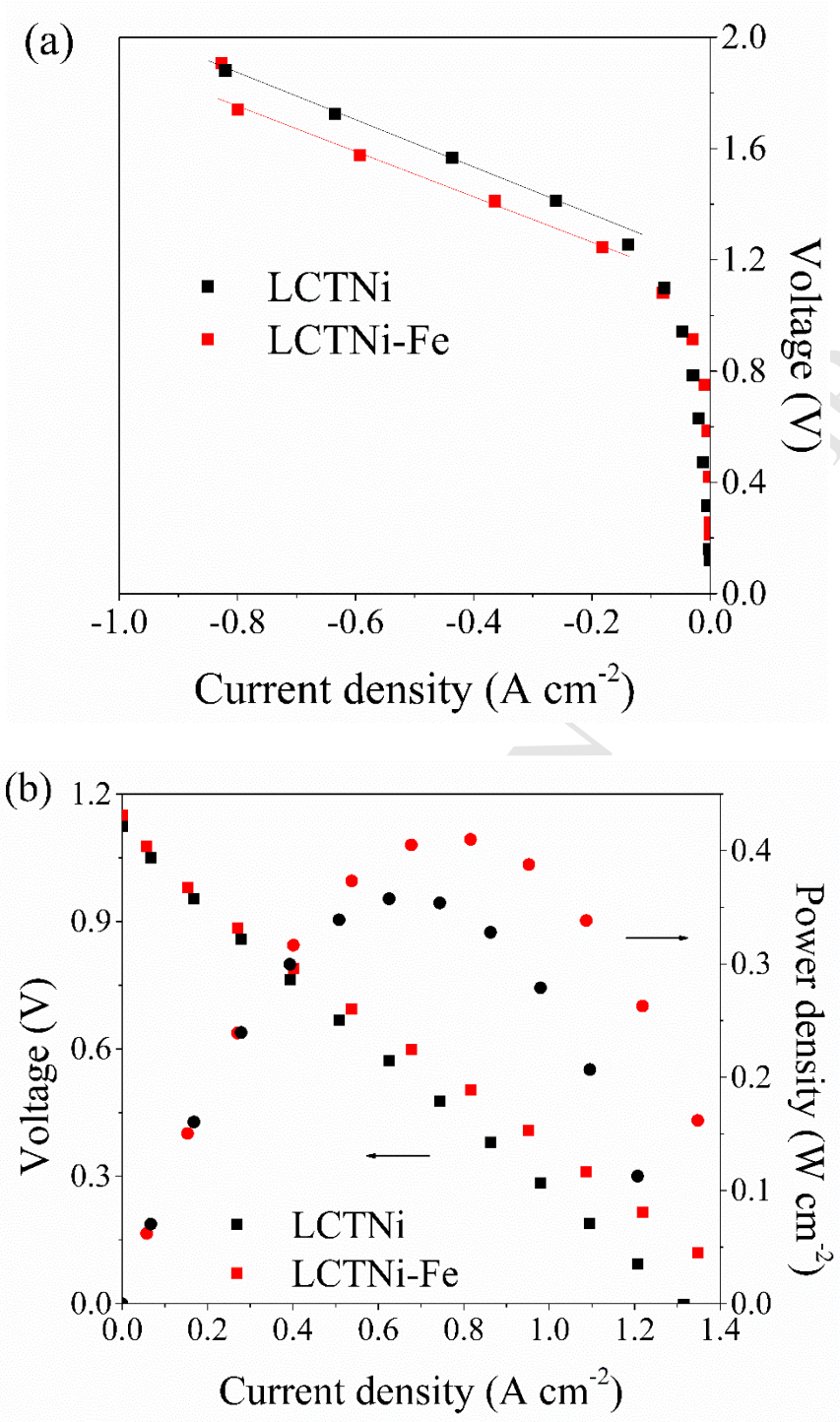

Figure 6. Current density vs. voltage and power density curves of a single cell with LCTNi or LCTNi-Fe electrode operated at 900 ºC in (a) electrolysis mode in 100% CO_2 and (b) fuel-cell mode in dry H_2